Published in final edited form as:
Contrast Media Mol Imaging. 2010 May ; 5(3): 162–170. doi:10.1002/cmmi.383.

High-Throughput Screening of Chemical Exchange Saturation Transfer MR Contrast Agents

Guanshu Liu[1,2], **Assaf A. Gilad**[1,2,3], **Jeff W.M. Bulte**[2,3,4,5], **Peter C.M. van Zijl**[1,2], and **Michael T. McMahon**[1,2,*]

[1]F.M. Kirby Research Center for Functional Brain Imaging, Kennedy Krieger Institute, Baltimore, Maryland [2]The Russell H. Morgan Department of Radiology and Radiological Sciences, Division of MR Research, Baltimore, Maryland [3]Cellular Imaging Section and Vascular Biology Program, Institute for Cell Engineering, Baltimore, Maryland [4]Department of Biomedical Engineering, Baltimore, Maryland [5]Department of Chemical & Biomolecular Engineering, Johns Hopkins University School of Medicine, Baltimore, Maryland

Abstract

A new high throughput (HT) MRI method for screening Chemical Exchange Saturation Transfer (CEST) agents is demonstrated, allowing simultaneous testing of multiple samples with minimal attention to sample configuration and shimming of the main magnetic field (B_0). This approach, which is applicable to diamagnetic (DIACEST), paramagnetic (PARACEST) and liposome (LIPOCEST) CEST agents, employs a set of inexpensive glass or plastic capillary tubes containing CEST agents put together in a cheap plastic tube holder, without need for liquid between the tubes to reduce magnetic susceptibility effects. In this setup, a image of direct water saturation spectra is acquired in order to map the absolute water frequency for each volume element (voxel) in the sample image, followed by an image of saturation transfer spectra to determine the CEST properties. Even though the field over the total sample is very inhomogeneous due to air/tube interfaces, the shape of the direct saturation spectra is not affected, allowing removal of susceptibility shift effects from the CEST data by using the absolute water frequencies from the map. As a result, quantitative information such as the mean CEST intensity for each sample can be extracted for multiple CEST agents at once. As an initial application, we demonstrate rapid screening of a library of 16 polypeptides for their CEST properties, but in principle the number of tubes is limited only by the available signal-noise-ratio, field of view and gradient strength for imaging.

Keywords

High throughput; MRI; CEST; B_0 correction

INTRODUCTION

Chemical Exchange Saturation Transfer (CEST) imaging has recently emerged as a novel MRI contrast mechanism that provides an attractive alternative to T_1 and T_2 contrast agents(1–5).

mcmahon@mri.jhu.edu.

SUPPORTING INFORMATION

Supporting Information includes the B_1 measurement data for our 15 mm RF coil, the technical details about our RGB color map construction for the 16-peptide library, the theoretical analysis of the relationship between accuracy of CEST measurement and a small B0 error at different saturation offset and saturation field strength.

CEST agents generally possess protons(6,7) or water molecules(8,9) that exchange rapidly with bulk water protons or molecules, respectively, although chemical exchange of other species such as Xe(10) can also be detected using saturation transfer. In a CEST study, image contrast is generated by selectively saturating the agent's exchangeable protons, resulting in an attenuation of the MRI signal of bulk water through the exchange transfer of saturation. Currently, CEST contrast agents are being explored for several biomedical applications, including direct cell labeling(11), gene expression(12), pH measurement(1,4,6,13,14), temperature mapping(15), metabolite quantification(16–18), drug delivery(19,20), and enzyme activity assessment(21,22). CEST compounds can be designed to contain distinguishable signals at multiple MRI frequencies (chemical shifts), enabling simultaneous detection of multiple agents(11,23). In addition, by removing the saturation pulse, T_2, T_2 *, and/or T_1-weighted images can be collected without CEST effects contaminating the images. In other words, CEST contrast is 'switchable', allowing simultaneous detection of multiple contrast types(24,25).

CEST-based MRI molecular imaging is a new field and there have been significant amounts of effort directed towards increasing the sensitivity and specificity of the available probes. There is an emerging need to discover better CEST probes for biological applications by screening a wide range of natural compounds(1), synthetic compounds(9) or even libraries of CEST active reporter genes(12,23). Unfortunately, the conventional approach for screening these agents is slow. Typically, a single NMR tube containing one (or sometimes two or three) CEST agents is used, while many experiments are needed to characterize the water saturation with regard to saturation offset (so-called z-spectrum analysis(26)) and also to measure the exchange rates for an agent by varying the saturation time (QUEST(6)), or saturation power (QUESP(6)). CEST images are extremely sensitive to variation in the B_0 field, which would seem to prohibit the application of multiplex methods, i.e. the use of multiple sample holders (27–32). The presumed problem is the presence of a high density of glass-fluid and air-glass interfaces(29), which results in water line broadening due to an apparent decrease in T_2* of the sample and wide shifts in the water resonant offsets. A common technique to reduce this effect is to fill the area surrounding the tubes with susceptibility matched fluids, such as Fluorinert FC-43(28,33), but this may still be insufficient for accurately characterizing CEST agents where small shifts may strongly impact the apparent CEST effects due to interference of direct saturation effects that have a strong frequency dependence, especially when in close proximity to the water signal. The range of water resonance shifts across all the samples strongly depends on the shimming condition, which can broaden the water signal from a single tube to the entire width of the acquired z-spectra past and conceal the CEST contrast. Despite the presence of large susceptibility changes associated with the number of air/glass/solution interfaces in our high throughput phantom, we demonstrate here that high-throughput (HT) CEST imaging can be accomplished using our protocol with just air between the tubes.

RESULTS

In order to improve the throughput, we develop a MRI–compatible sample holder (Fig. [1A]), on which tubes are carefully arranged (Fig. [1B]) so that each can be unambiguously localized in the MRI image (Fig. [1C]). However, immense susceptibility differences arise due to the high density of air/glass/solution interfaces. For example, Fig. [1D] shows that, when a typical automatic shimming procedure was used, the B_0 inhomogeneity across the entire 18 capillaries was measured as high as 3.5 ppm with some pixels shifted up to 2 ppm from water resonant frequency, as measured with our WAter Saturation Shift Reference (WASSR) B_0 mapping method. To determine our ability to correct the B_0 inhomogeneity in CEST images and reconstruct z-spectra in a sample of multiple tubes separated by air, a phantom consisting of seven myo-inositol samples was constructed (Fig. [2A]). Myo-inositol was chosen because B_0 frequency errors would result in large errors in CEST contrast due to the small chemical

shift difference between OH protons and water protons (0.8 ppm). In order to test the dynamic range of our correction scheme, samples of different pH were prepared so that the MTR_{asym} (CEST contrast as defined in Materials section) would vary from 0 to 0.5, which is the range that most *in vitro* CEST studies have used previously. In addition, both shimmed and de-shimmed conditions were studied. The *ad hoc* extreme deshimming condition broadened the water line about 10-fold for the whole sample (160 Hz or 0.32 ppm before, and 1750 Hz or 3.5 ppm after deshimming) and 2.5-fold for a single representative capillary (Fig [2D], 66 Hz before and 150 Hz after deshimming).

Fig. [2C] illustrates WASSR spectra produced for a single capillary tube (myo-inositol, pH 5) under shimmed and de-shimmed conditions. Even though the water shift was as large as 1800 Hz downfield when shimmed poorly (Fig. [2D]), this did not affect the shape or width of the direct saturation reference spectrum (full width at half maximum FWHM = 99 Hz for shimmed sample verse 106 Hz for the deshimmed sample) as shown in Fig. [2C]. Such field shifts would normally be disastrous for CEST analysis, but the WASSR approach allows one to correct for the images. When computing the corrected CEST z-spectra for both shimming conditions (Fig. [2E]), the MTR_{asym} at 0.8 ppm was corrected from 26.2% to 43.2% for the shimmed sampled and from 5.9% to 44.5% for the deshimmed sample. In Fig. [2F], the CEST contrast for all seven capillary tubes is given, showing excellent agreement between the two shimming conditions, even at pH 7.8, where the CEST effect disappears due to the proton exchange rate becoming too fast compared to the chemical shift separation. These results demonstrate that the B_0 inhomogeneity effect can be corrected for even when the sample was shimmed very ‘poorly’.

In order to investigate the reproducibility of our method, we carried out CEST measurements on two protamine sulfate solutions with concentrations of 0.2 mM and 0.98 mM at pH 7.3, and constructed a phantom consisting of six capillaries for each concentration, with the distribution of the tubes shown in Fig. [3A]. Five measurements of 30 min each were conducted with an interval of three hours between them. When comparing the CEST contrast at 1.8 ppm as a function of position in the holder (Fig. [3B]) and collection time (Fig. [3C]), the computed MTR_{asym} values did not show any statistical differences between measurements (two-tailed paired student t-test, n=5, $P > 0.1$), indicating that measurements were repeatable over 12 hrs and across the sample holder. The intra-tube variation was 0.4% under these high SNR conditions.

The HT-CEST method was also applied to measure the pH dependency of uracil proton MTR_{asym} (Fig. [4]) in a 20 mM solution in PBS. The intra-sample standard deviation for the ring NH proton (at 5.4 ppm) was < 0.6%, which is lower than found previously for myo-inositol (< 2.2% at 0.8 ppm in Fig. [2F]), and similar to protamine sulfate (<0.4% at 1.8 ppm in Fig. [3B]). This is reflected in the error bars displayed for all the different data points in Fig. [4B]. Even for the points displaying small amounts of CEST contrast, such as pH 7.3 and 7.6, there is sufficient CNR per voxel (CNR per voxel=2.23 and 4.2), to reliably detect the CEST contrast.

Using the same HT-holder, sixteen DIACEST polypeptides (each twelve-residues long) were scanned simultaneously (Fig. 5) on our 11.7T scanner. This peptide library was designed for each peptide to have different ratios of three chemically different exchangeable protons, namely amide (NH), guanidyl (NH_2) and hydroxyl (OH), which resonate at 3.6 ppm (1800 Hz), 1.8 ppm (900 Hz) and 0.8 ppm (400 Hz) with respect to water, respectively. We used a saturation pulse field strength of 200 Hz, in order to obtain the Z-spectra of all of these. Plots of the MTR_{asym} for each tube (representative data Fig. [5 A–C]) reveal the different CEST profiles for each peptide. By generating MTR_{asym} maps at 3 offset frequencies (3.6 ppm, 1.8 ppm and 0.8ppm; Fig 5D–F) and super-imposing the three different images (as described in the

Supporting Information), we can generate RGB images (Fig. [5G]) showing a characteristic color for each peptide.

DISCUSSION

The main goal of this study was to design an experimental setup for simultaneous screening of multiple CEST contrast agents with the goal of more efficient evaluation of large sets of potential compounds. The HT-setup requires only small sample volumes (20 μl to 50 μl), much less than the typical 300 μl for a 5 mm NMR tube. Because the samples experience the same experimental parameters (e.g. saturation pulse power calibration, main field strength, pulse sequence timings, and receiver gain), comparison between them should be more accurate than when scanning them individually. The system is inexpensive and uses a simple B_0 shift compensation scheme to ensure reliable data.

At first impression, the presence of many high-density glass-air interfaces is expected to lead to an uncorrectable variance in B_0 across the sample,(29) as seems to be confirmed by the field frequency map in Fig. [1D]. Such B_0 inhomogeneities, if left uncorrected, can erroneously increase or reduce CEST contrast.(12,34) For example, errors of −98 Hz (−0.19 ppm) would change the MTR_{asym} from 43.2% (Fig. [2E]) to 26.2% for 31.25 mM myo-inositol at pH 5. In order to first determine the B_0 inhomogeneity and then correct it, we use the WASSR method (originally described by Kim and co-workers at 3T(35)) with several changes which include the use of a different fit function for determining the B_0 map and new parameters (*i.e.* saturation offset interval, saturation pulse field strength and saturation pulse duration) which were optimized to account for the larger variations in B_0 inhomogeneity found on our high field scanners. The ability to reproduce CEST contrast accurately is strongly affected by the chemical shift of the exchangeable proton (Δω, in Hz) and and the other parameters listed above used for producing a WASSR B_0 map. Direct interpolation of the CEST spectra could also be used(36), however the B_0 map produced by this will be less accurate due to the increased width of the water peak in the Z-spectra due to the higher saturation power used to for CEST contrast generation. We were interested in determining the error in MTR_{asym} (CEST contrast) experimentally for a range of conditions, and in particular we have tested this at three different chemical shifts from water, 5.4 ppm (ring NH), 1.8 ppm (guanidyl NH_2) and 0.8 ppm (OH). The worst case, 2.2% error in MTR_{asym}, is found for the CEST signal of pH 5 myo-inositol when a 3.6 μT saturation field strength was used. At the OH frequency of 0.8 ppm, the MTR_{asym} data is particularly sensitive to offset errors because the direct saturation of water is so high (~30%) and this saturation varies with frequency (the slope is ~0.15 %/Hz). As a result, an error in B_0 of 7 Hz would produce a 2.2 % change in the direct saturation component of the signal loss, and of course there will be an error in the CEST component as well. The direct saturation sensitivity to B_0 reduces as the exchangeable proton is moved further away from water, for example in the MTR_{asym} measurements on compounds containing 5.4 ppm imidazole NH protons the uncertainty is reduced to ~ 0.4% because at this frequency the same saturation pulse produces only a ~1.6% drop in water signal (as opposed to 30%) and the slope is ~0.005 %/Hz. This is reflected in the smaller error bars in Fig. [4B]. For more details on the relationship between the chemical shift and errors in MTR_{asym}, see the supporting information. There we derive an expression which relates the exchangeable proton chemical shift, saturation field strength, WASSR B_0 map errors to the error in CEST contrast.

When saturation transfer data are collected on CEST agents dissolved in buffer, there are two sources of water signal loss: direct saturation of the water line by the saturation pulse, and indirect chemical exchange saturation transfer signal loss (CEST effect). Higher direct saturation, produced by higher saturation field strength or a closer chemical shift position to water, impairs the measurement accuracy by lowering the signal-noise-ratio. As a result, the uncertainty in signal loss (or MTR_{asym}) will increase in proportion to the amount of direct

saturation of water. In our study we have shown that in order to keep the uncertainty in CEST contrast under 3%, the saturation B_1 strength should be kept at or below a value, which produces a 36% direct saturation effect at the position of the exchangeable peak. We have chosen to use 3% as a threshold because CEST contrast is often in the range of 30%, and so a 3% error is a 10% error in the total contrast. Using higher saturation field strengths will not be relevant for *in vivo* studies because the non-CEST water signal loss will be much greater than *in vitro* due to the shorter T_2 present in tissues than in buffer and the additional magnetization transfer effects produced by macromolecules and metabolites. In this respect, it is also useful to characterize the CEST effects in crosslinked BSA or agar for those CEST agents that will be applied *in vivo*. The methods we have described are applicable, and additional tubes containing both CEST agent and agar (or crosslinked BSA) can be added to a high throughput phantom without any modifications to the method or acquisition parameters we have described.

In general, CEST effects at large chemical shifts from water are more desirable, indicating that paramagnetic CEST (PARACEST) agents(4,9) might be less susceptible to errors in B_0 correction, provided that the direct saturation is no higher than the compounds measured above. In these cases the error in the CEST contrast measurement will be related instead to the width of the CEST dip in the Z-spectrum which depends on the saturation field strength. As the CEST dip widens with increasing saturation strength, the CEST contrast measurement will become more tolerant to B_0 variation, with the error inversely related to this width. We present expressions in the supporting information, S.3 which can be used as a guide for specific applications. Although we did not perform a detailed analysis of the conditions relevant for PARACEST agents, the inhomogeneities produced by the number of glass/air/solution interfaces in phantoms will still require B_0 field correction, especially for a large number of samples as the B_0 inhomogeneity across the entire phantom will generally increase with the number of interfaces. The expression derived in the supporting information (S.3) can be used as a guide for these agents. This indicates that our method is also critical for high throughput screening of PARACEST agents by providing accurate B_0 correction without needing too much measurement time and with the same image artifacts present in the CEST images (unlike the gradient echo based maps). Our method will also be useful for the development of LIPOCEST agents, which possess exchangeable protons with similar chemical shifts and exchange rates to the DIACEST agents we tested in this study. A way to reduce the error further would be increase the accuracy of the B_0 shift map, at the expense of increasing the imaging time. For example, the frequency increment could be decreased to 25 Hz and the saturation field strength reduced to 0.25 μT at the expense of doubling the B_0 shift map image collection time.

Collecting a separate low power Z-spectrum is not the only way to determine the B_0 shift map. Another method to determine the B_0 shift map would be to interpolate the high saturation power Z-spectra using smoothing-splines(36), however this will not measure the B_0 shift map as accurately as the method we propose, because the Z-spectra are broadened by the higher saturation field strength, resulting in larger errors. A third method that has been proposed(37) would be to collect a typical B_0 field map(38) using different gradient echo times, however the field map images will then contain different field-based image distortions due to the different acquisition schemes, and also might not be able to measure the large frequency shifts we have seen in the high throughput phantoms.

In addition to B_0 inhomogeneity, spatial B_1 variation also should be considered for the quantification of CEST contrast.(37) Our B_1 measurements (in Supporting Information, S.1) indicated that the B_1 homogeneity for the tubes in this HT CEST phantom is >95%. Moreover, based on simulations and measurements, the effects caused by minor B_1 variation can be considered negligible when the applied B_1 is <5% from the optimal B_1.(39) As shown in Fig. [3], we were able to distribute samples in different positions in the holder with minimal disturbance in measured CEST contrast.

The HT CEST technique has two main advantages in screening libraries of CEST contrast agents: 1) it allows a quantitative comparison of the sensitivity for all agents at the same saturation and acquisition conditions and 2) it can simultaneously determine the saturation frequency spectrum for each sample (11,23), which is what allows the agents to be discriminated from each other in the MR images. There is a loss in SNR from using smaller sample sizes than used typically for NMR and also from obtaining the Z-spectra using imaging instead of spectroscopy, but we have found the SNR to be more than adequate using the 20 uL sample size and spatial resolution, slice thickness described in the Materials section. In the present study, we applied the HT CEST technique to screen a library of peptide CEST agents with multiple distinguishable CEST saturation frequency spectra. The RGB CEST image shows that 6 peptides, $(KS)_6$, $(DSSS)_3$, $(DTT)_4$, $(DTTTTT)_2$, $(RT)_6$ and $(RTTT)_3$, of the 16-peptide library were determined to have distinguishable RGB color saturation frequency spectra by modulating the CEST contrast at three different saturation offsets for the agents. We used a saturation $\omega_1/2\pi = 200$ Hz, on our 11.7 T scanner, which results in 900 Hz and 400 Hz separating the NH from NH_2 and NH_2 from OH respectively. This allows the three contrasts to be relatively independent from each other. This proof-of-concept study implies that by altering the amino acid composition, a number of peptide contrast agents can be designed with distinguishable CEST spectra, potentially allowing the separate monitoring of each of the contrast agents via MRI. New biomedical applications such as the simultaneous detection of expression of multiple genes using MRI in vivo could then be feasible(12,23).

It should be noted that the sample throughput and required sample volumes are not limited to what we describe above, and can be improved by using scanners with larger FOV, improved coils, and improved gradient performance, with the determining factor for sample volume being the signal to noise ratio per voxel. In the current setup, voxel SNR (>150) at a spatial resolution of 100×200 μm in-plane indicates that even smaller tubes can be used instead of the capillaries which were 60 voxels. Another alternative would be to use a bigger RF coil and larger FOV.

CONCLUSIONS

This study demonstrates a HT MRI method for screening CEST contrast agents *in vitro*. The proposed method is fast, sensitive and reproducible even in presence of severe line broadening and water resonance offset shifting (B_0 inhomogeneity). The setup does not require a uniform magnetic field and no fluid is needed between the capillary tubes, because the acquisition of saturation spectra provides an inherent means for efficient B_0 correction. The applicability of this method was verified using protamine sulfate, uracil, myo-inositol and a peptide library of 16 agents containing different amounts of exchangeable protons resonating at 3.6 ppm, 0.8 ppm and 1.8 ppm, indicating applicability over a broad range of diamagnetic chemical shifts. For the library, an average acquisition time of only 3.2 minutes per sample per z-spectrum was needed. This method can greatly facilitate the screening of CEST contrast agents, which is particularly relevant in light of expanding efforts towards the development of more specific and higher efficiency CEST agents for preclinical research and eventual clinical trials.

EXPERIMENTAL

Multi-Sample Holder

The high throughput phantoms were arranged and inserted into a 15 mm Birdcage RF coil as shown in Figs. [1A] and [1B]. The capillary tube holder was constructed by cutting a 1536 well tissue culture plate [purchased from Corning Inc, Corning, NY] to fit within the coil. Subsequently, 1 mm OD capillary tubes (Fisher, Hanover Park, IL) were mounted upright with the maximal capacity depending on the coil size (i.e. field of view of the scanner). For our high-resolution 11.7 T scanner birdcage coil the capacity was about 25 tubes, but this can straightforwardly be expanded to hundreds of tubes in a larger imager with a body coil or head

coil based field of view (FOV) and sufficient gradient strength and signal to noise for high-resolution imaging. Capillaries were positioned in the holder without fluid between the tubes and arranged as shown in Fig. [1B]. In this example, 18 tubes were used to accomplish an anisotropic arrangement of samples in which each can be easily identified in the MRI image through recognition of the pattern. Sample volumes ranging from 20 μl to 50 μl were used, depending on the amount of sample available. Smaller volumes required more precise alignment of the tubes vertically in the RF coil, so for convenience we used 50 μl whenever possible.

MR Image Collection

All MRI images were acquired at 310 K using an 11.7 T Bruker Avance system. Both shimmed and de-shimmed conditions were generated for demonstration purposes. For the shimmed experiment, the B_0 field was shimmed manually to 2^{nd} order using the shimming toolbox in Paravision Version 3.0.2 (Bruker Biospin Co., Billerica, MA). In the de-shimmed condition, the 1^{st} order shim currents (X, Y and Z) were mis-set. A modified Rapid Acquisition with Relaxation Enhancement (RARE) sequence including a saturation pulse was used to acquire saturation images as a function of irradiation frequency (generating images that contain a so-called z-spectrum or saturation spectrum or CEST spectrum in each voxel). A slice thickness of 0.5 mm was used for all images. The typical imaging parameters were: effective TE= 4.3 ms, RARE factor =16, acquisition bandwidth =100 kHz, and an acquisition matrix size of 128×64. Depending on the number of tubes in the phantom, the field of view was varied from 13×13 mm to 22×22 mm resulting in an in-plane resolution of 101×203 μm to 172×343 μm. Two types of saturation images were acquired: frequency map images used for mapping the spatial B_0 distribution for the phantoms and CEST images which we use to determine the contrast properties. Unless mentioned otherwise, the number of averages (NA) was 2, and the corresponding acquisition times per frequency point were 48 seconds for CEST images (TR=6.0 s) and 17.6 seconds for frequency maps (TR=2.2 s).

Acquisition of saturation based B_0 maps—Recently, it was shown that the z-spectra can be acquired using a low power, short saturation pulse can be utilized to map the absolute water frequencies for each voxel in an image, an approach termed WAter Saturation Shift Reference (WASSR) mapping(35). Because the saturation pulse is short and weak, CEST and conventional magnetization transfer (MT) (as reviewed by Henkelman and co-workers(40)) contributions to the z-spectra are minimized and only direct water saturation spectra are obtained. Such spectra are inherently symmetric(41) around the water frequency and can thus be used for "absolute B_0" mapping.(35) In our study, we used a saturation pulse length (t_{sat}) of 200 ms, saturation field strength (B_1) of 0.5 μT (21.3 Hz) and saturation frequency increment of 50 Hz (spectral resolution = 0.1 ppm) to collect such WASSR images prior to CEST imaging. The field strength, saturation time, and frequency increment was chosen based on Monte Carlo simulations as was previously described(35). Using this sampling resolution and saturation strength, the direct saturation dip is defined by 3 or more points will lead to errors in the B_0 map of < ±3 Hz which was deemed sufficient for proper analysis of the current samples. To accurately determine the B_0 shift for each voxel, the saturation offset should be incremented over the entire range of water frequencies in the FOV, which can be pre-determined by collecting a water spectrum of the complete sample. For the shimmed samples, the saturation offset ranged from −2 ppm to + 1.4 ppm with respect to water (3.4 ppm bandwidth). For the deshimmed phantoms, this bandwidth was about 5 ppm. We kept an identical image readout between the frequency map and CEST images to allow easy co-registration between CEST and WASSR images, and to retain the same image artifacts. The total scan times required to generate this WASSR absolute B_0 map varied from 10 minutes for shimmed phantoms to 14.7 minutes for deshimmed phantoms.

CEST Weighted Images—All acquisitions used t_{sat} = 4 sec and a frequency increment of 0.2 ppm. Two B_1 saturation fields were used, B_1 = 4.7 μT (200 Hz) for CEST offsets > 3.6 ppm, and B_1 = 3.6 μT (150 Hz) for CEST offsets < 2 ppm. The principle is to use high saturation field strengths to enhance the CEST contrast while minimizing the direct saturation at the exchangeable proton chemical shift. In particular, the saturation offset was discretely swept from −7 ppm to +7 ppm (with regard to the chemical shift of water that is referenced to 0ppm) at B_1 = 4.7 μT (200 Hz) for uracil samples. For protamine sulfate samples, the saturation offset was discretely swept from −5 ppm to +5 ppm, B_1 = 3.6 μT (153 Hz). For myo-inositol samples, the saturation offset was incremented from −3 ppm to +3 ppm, B_1 = 3.6 μT (153 Hz). For polypeptide samples, the saturation offset was discretely swept from −5 ppm to +5 ppm, B_1 = 1.2 – 4.7 μT (50–200 Hz). Notice that, when using a clinical imager for the consecutive WASSR-CEST acquisitions, the automated prescan for shimming and frequency adjustment has to be turned off between the scans. This is not an issue for high-resolution spectrometers, where offsets and shims are not adjusted automatically before each scan.

Spectroscopic Data Collection—A point-resolved spectroscopy (PRESS) sequence was used to measure the bandwidth of water spectra under different shimming conditions. The voxel size was chosen to be either 13×13×9.5 mm^3 to cover the entire FOV, or 0.5×0.5×0.5 mm^3 to cover a single capillary tube (as shown in Fig. [2A]). TR/TE was 1000/16.7 ms, using a spectrum acquisition size of 8192 points and a sweep width of 10,080 Hz. For the de-shimmed phantom we needed to average 512 scans due to the width of the water line, giving a total scan time of 8.5 min. Under shimmed conditions, 4 averages sufficed. 1H NMR spectra were processed using 1D FT with line-broadening factor of 2, followed by phase and baseline correction using Topspin software package (Bruker Biopsin Co. Billerica, MA).

Image Post-processing and Analysis

Generation of Saturation-Based B_0 Shift Maps—All processing was performed using custom-written scripts in Matlab (Mathworks, Natick, MA). No zero-filling was used to improve the spatial resolution of MRI images. WASSR images were fit to find the frequency offset (Δω) for each voxel and generate a saturation-based B0 shift map. Previously Mulkern and Williams derived an analytic expression for the steady state saturation lineshape of the longitudinal magnetization (M_z^{SS}), given by(41):

$$M_z^{SS} = \frac{M_z^0}{1+(\frac{\omega_1}{\Delta\omega})^2(\frac{T_1}{T_2})} \quad [1]$$

Here M_z^0 is the initial longitudinal magnetization, ω_1 is the strength of the applied RF pulse which is resonating at Δω (frequency with respect to the proton center frequency). The assumption of Eq. [1], $1/T_2 \ll \Delta\omega$, is generally satisfied for CEST contrast measurements at high field. In order to fit the images and determine the absolute field map, we need to compare the experimental signal intensities ($S_{exp}(x, y)$) for each voxel in all the saturation based images using Eq. [2]:

$$S_{exp}(x,y) = \left\{ \eta^2 + \left[\frac{M_0(x,y)}{1+(\frac{\omega_1(x,y)}{\Delta\omega(x,y)-\delta\omega_0(x,y)})^2 \frac{T_1(x,y)}{T_2(x,y)}} \right]^2 \right\}^{1/2} \quad [2]$$

This equation is slightly modified to take into account the B_0 inhomogeneity with respect to the reference frequency ($\delta\omega_0(x, y)$) and the experimental noise (η) in the magnitude image.

Experimentally, η was estimated from the mean signal of air within the image. The images were fit voxelwise to Eq. [2] using the non-linear fitting function (*lsqcurvefit*) in Matlab, with M_0, $\delta\omega_0$ and $(\frac{T_1}{T_2}\omega_1^2)$ as the free parameters. In order to reduce the processing time, the images were masked using a signal to noise ratio threshold of SNR ≥ 30. The absolute water resonant frequency (B_0 shift) map was obtained by plotting $\delta\omega_0$ (x,y) for each voxel.

CEST Image Analysis—The CEST weighted images were then corrected voxel wise using the WASSR absolute frequency map determined above. The irradiating frequencies were corrected using:

$$\Delta\omega(x,y)_{\text{corrected}}=\Delta\omega(x,y)-\delta\omega_0(x,y) \quad [3]$$

The Saturation weighted images were then interpolated with cubic-spline fitting to obtain the signal intensity $S_{interp}(x, y, \Delta\omega)$ at the desired offsets $\Delta\omega_{\text{desired}}$, using the following expression:

$$S_{interp}(x,y,\Delta\omega)=spline(\Delta\omega_{uncorrected}, S_{\exp}(x,y,\Delta\omega_{uncorrected}), \Delta\omega_{\text{desired}}(x,y)) \quad [4]$$

For ROI analysis, ROI masks were manually drawn, and with the mean intensity then used for plotting z-spectra (relative water saturation $S^{\Delta\omega}/S_0$ as a function of saturation frequency offset with respect to water). The CEST contrast was quantified by determining the asymmetry in the magnetization transfer ratio (MTR_{asym}) as defined by the expression:

$$MTR_{asym}=\frac{\left(S^{-\Delta\omega}-S^{+\Delta\omega}\right)}{S^{-\Delta\omega}} \quad [5]$$

where $S^{+\Delta\omega}$ and $S^{-\Delta\omega}$ are the signal intensities with a saturation at frequency Δω downfield and Δω upfield from the water proton resonance frequency respectively.

The signal to noise ratio (SNR) was defined by the expression:

$$SNR=\frac{S_{sample}^{-\Delta\omega}}{\sigma_{noise}^{-\Delta\omega}} \quad [6]$$

where $S_{sample}^{-\Delta\omega}$ and $\sigma_{noise}^{-\Delta\omega}$ are the mean signal intensities from the sample region and the standard deviation of the noise region outside the tubes respectively, with a saturation pulse applied at a frequency Δω upfield from the water proton resonance frequency.

The contrast to noise ratio CNR was calculated using:

$$CNR=\frac{\left(S^{-\Delta\omega}-S^{+\Delta\omega}\right)}{\sqrt{2}\sigma} \quad [7]$$

where σ is the standard deviation of the noise and the $\sqrt{2}$ comes from MTR_{asym} images being difference images.

Chemicals and Phantom Preparation

Uracil (U), protamine sulfate (average Mw=5.1 kD) and myo-inositol were purchased from Sigma-Aldrich (St. Louis, MO). The chemicals were dissolved in 10 mM phosphate buffered saline (PBS) at the desired concentrations, i.e. 20 mM for uracil, 0.2 and 0.98 mM for protamine sulfate, and 31.25 mM for myo-inositol respectively. The solutions were then titrated to pH 7.3 for all studies using 1 M hydrogen chloride and 1 M sodium hydroxide, except the pH dependency studies of uracil and myo-inositol, where solutions were adjusted from pH 5.0 to pH 7.8. In the peptide library study, the twelve residue polypeptides, $(KS)_6$, $(KSSS)_3$, $(RT)_6$, $(RTT)_4$, $(RTTT)_3$, $(TK)_6$, $(TTK)_4$, $(DTT)_4$, $(ETT)_4$, $(TTTK)_3$, $(DTTT)_3$, $(ETTT)_3$, $(TTTTTK)_2$, $(DTTTTT)_2$, $(ETTTTT)_2$, $(DSSS)_3$, $(DSSSSS)_2$, (K = lysine, S = Serine, R = Arginine, T = Threonine, E = Glutamate, D = aspartate) were purchased from Bio S&T Inc. (Montreal, Quebec) and Sigma Genosys (The Woodlands, TX). The molecular weights of the peptides varied from 1.12 to 1.56 kD. The concentrations of non-arginine-containing peptides were set to 2.5 mg/mL in PBS (~2 mM), while the concentrations of arginine-containing peptides were set to 1.25 mg/mL (~0.9 mM). All the solutions were titrated to pH 7.3 using 1M hydrogen chloride and 1M sodium hydroxide. All samples were placed in 1 mm capillary tubes and arranged as described in the phantom setup.

Supplementary Material

Refer to Web version on PubMed Central for supplementary material.

Acknowledgments

Supported by NIH grants R21 EB005252, EB008769-01A1, NS065284-01 and K01 EB006394.

REFERENCES

1. Ward KM, Aletras AH, Balaban RS. A new class of contrast agents for MRI based on proton chemical exchange dependent saturation transfer (CEST). Journal of Magnetic Resonance 2000;143(1):79–87. [PubMed: 10698648]
2. Sherry AD, Woods M. Chemical Exchange Saturation Transfer Contrast Agents for Magnetic Resonance Imaging. Annual Review of Biomedical Engineering 2008;10:391–411.
3. Zhou J, van Zijl PC. Chemical exchange saturation transfer imaging and spectroscopy. Progress in Nuclear Magnetic Resonance Spectroscopy 2006;48:109–136.
4. Aime S, Barge A, Delli Castelli D, Fedeli F, Mortillaro A, Nielsen FU, Terreno E. Paramagnetic lanthanide(III) complexes as pH-sensitive chemical exchange saturation transfer (CEST) contrast agents for MRI applications. Magnetic Resonance in Medicine 2002;47(4):639–648. [PubMed: 11948724]
5. Vinogradov E, He H, Lubag A, Balschi JA, Sherry AD, Lenkinski RE. MRI detection of paramagnetic chemical exchange effects in mice kidneys in vivo. Magnetic Resonance in Medicine 2007;58(4):650–655. [PubMed: 17899603]
6. McMahon MT, Gilad AA, Zhou J, Sun PZ, Bulte JW, van Zijl PC. Quantifying exchange rates in chemical exchange saturation transfer agents using the saturation time and saturation power dependencies of the magnetization transfer effect on the magnetic resonance imaging signal (QUEST and QUESP): Ph calibration for poly-L-lysine and a starburst dendrimer. Magnetic Resonance in Medicine 2006;55(4):836–847. [PubMed: 16506187]
7. Ling W, Regatte R, Navon G, Jerschow A. Assessment of glycosaminoglycan concentration in vivo by chemical exchange-dependent saturation transfer (gagCEST). Proceedings of the National Academy of Sciences 2008;105(7):2266.
8. Enzo Terreno DDC, Elisabetta Violante, Honorius M†H†F, Sanders NicoA†J†M, Sommerdijk Silvio Aime. Osmotically Shrunken LIPOCEST Agents: An Innovative Class of Magnetic Resonance Imaging Contrast Media Based on Chemical Exchange Saturation Transfer. Chemistry - A European Journal 2009;15(6):1440–1448.

9. Zhang S, Merritt M, Woessner DE, Lenkinski RE, Sherry AD. PARACEST Agents: Modulating MRI Contrast via Water Proton Exchange Accounts of Chemical Research. 2003;36:783–790.
10. Schroder L, Lowery TJ, Hilty C, Wemmer DE, Pines A. Molecular imaging using a targeted magnetic resonance hyperpolarized biosensor. Science 2006;314(5798):446–449. [PubMed: 17053143]
11. Aime S, Carrera C, Delli Castelli D, Geninatti CrichS, Terreno E. Tunable imaging of cells labeled with MRI-PARACEST agents. Angew Chem Int Ed 2005;44:1813–1815.
12. Gilad AA, McMahon MT, Walczak P, Winnard PT Jr. Raman V, van Laarhoven HW, Skoglund CM, Bulte JW, van Zijl PC. Artificial reporter gene providing MRI contrast based on proton exchange. Nature Biotechnology 2007;25(2):217–219.
13. Zhou J, Lal B, Wilson DA, Laterra J, van Zijl PC. Amide proton transfer (APT) contrast for imaging of brain tumors. Magnetic Resonance in Medicine 2003;50(6):1120–1126. [PubMed: 14648559]
14. Sun P, Zhou J, Sun W, Huang J, van Zijl P. Detection of the ischemic penumbra using pH-weighted MRI. Journal of Cerebral Blood Flow & Metabolism 2006;27(6):1129–1136. [PubMed: 17133226]
15. Li AX, Wxojciechowski F, Suchy M, Jones CK, Hudson RHE, Merton RS, Bartha R. A sensitive PARACEST contrast agent for temperature MRI: EU3+DOTAM-Glycine (Gly)-Phenylalanine (Phe). Magnetic Resonance in Medicine 2008;59(2):374–381. [PubMed: 18228602]
16. Zhang S, Trokowski R, Sherry AD. A paramagnetic CEST agent for imaging glucose by MRI. Journal of the American Chemical Society 2003;125(50):15288–15289. [PubMed: 14664562]
17. Liu G, Li Y, Pagel MD. Design and characterization of a new irreversible responsive PARACEST MRI contrast agent that detects nitric oxide. Magnetic Resonance in Medicine 2007;58(6):1249–1256. [PubMed: 18046705]
18. Huang C, Morrow J. A PARACEST Agent Responsive to Inner-And Outer-Sphere Phosphate Ester Interactions for MRI Applications. J Am Chem Soc 2009;131(12):4206–4207. [PubMed: 19317496]
19. Castelli DD, Terreno E, Cabella C, Chaabane L, Lanzardo S, Tei L, Visigalli M, Aime S. Evidence for in vivo macrophage mediated tumor uptake of paramagnetic/fluorescent liposomes. NMR in Biomedicine. 2009
20. Langereis S, Keupp J, van Velthoven JLJ, de Roos IHC, Burdinski D, Pikkemaat JA, GruÃàll H. A Temperature-Sensitive Liposomal 1H CEST and 19F Contrast Agent for MR Image-Guided Drug Delivery. Journal of the American Chemical Society 2009;131(4):1380–1381. [PubMed: 19173663]
21. Yoo B, Pagel MD. A PARACEST MRI Contrast Agent To Detect Enzyme Activity. Journal of the American Chemical Society 2006;128(43):14032–14033. [PubMed: 17061878]
22. Chauvin T, Durand P, Bernier M, Meudal H, Doan B, Noury F, Badet B, Beloeil J, Toth E. Detection of enzymatic activity by PARACEST MRI: a general approach to target a large variety of enzymes. Angew Chem Int Ed 2008;47(23):4370.
23. McMahon MT, Gilad AA, DeLiso MA, Berman SM, Bulte JW, van Zijl PC. New "multicolor" polypeptide diamagnetic chemical exchange saturation transfer (DIACEST) contrast agents for MRI. Magnetic Resonance in Medicine 2008;60(4):803–812. [PubMed: 18816830]
24. Gilad AA, van Laarhoven HW, McMahon MT, Walczak P, Heerschap A, Neeman M, van Zijl PC, Bulte JW. Feasibility of concurrent dual contrast enhancement using CEST contrast agents and superparamagnetic iron oxide particles. Magnetic Resonance in Medicine 2009;61(4):970–974. [PubMed: 19189296]
25. Aime S, Castelli DD, Lawson D, Terreno E. Gd-Loaded Liposomes as T1, Susceptibility, and CEST Agents, All in One. Journal of the American Chemical Society 2007;129(9):2430–2431. [PubMed: 17288421]
26. Bryant R. The Dynamics of Water-Protein Interactions. Annual Reviews in Biophysics and Biomolecular Structure 1996;25(1):29–53.
27. Wang H, Ciobanu L, Edison AS, Webb AG. An eight-coil high-frequency probehead design for high-throughput nuclear magnetic resonance spectroscopy. Journal of Magnetic Resonance 2004;170(2):206–212. [PubMed: 15388082]
28. MacNamara E, Hou T, Fisher G, Williams S, Raftery D. Multiplex sample NMR: an approach to high-throughput NMR using a parallel coil probe. Analytica Chimica Acta 1999;397(1–3):9–16.
29. Banas EM. "Multi-cloistered" NMR Cells. Applied Spectroscopy 1969;23:281.

30. Reetz MT, Tielmann P, Eipper A, Ross A, Schlotterbeck G. A high-throughput NMR-based ee-assay using chemical shift imaging. Chemical Communications (Cambridge, United Kingdom) 2004 Dec;: 1366–1367.

31. Perez JM, Josephson L, O'Loughlin T, Hogemann D, Weissleder R. Magnetic relaxation switches capable of sensing molecular interactions. Nature Biotechnology 2002;20(8):816–820.

32. Ross A, Schlotterbeck G, Senn H, von Kienlin M. Application of chemical shift imaging for simultaneous and fast acquisition of NMR spectra on multiple samples. Angew Chem Int Ed 2001;40 (17):3243–3245.

33. Olson DL, Peck TL, Webb AG, Magin RL, Sweedler JV. High-Resolution Microcoil H-1-Nmr for Mass-Limited, Nanoliter-Volume Samples. Science 1995;270(5244):1967–1970.

34. Jones C, Schlosser M, van Zijl P, Pomper M, Golay X, Zhou J. Amide proton transfer imaging of human brain tumors at 3T. Magnetic Resonance in Medicine 2006;56(3):585. [PubMed: 16892186]

35. Kim M, Gillen J, Landman BA, Zhou J, van Zijl PCM. WAter Saturation Shift Referencing(WASSR) for chemical exchange saturation transfer experiments. Magnetic Resonance in Medicine 2009;61 (6):1441–1450. [PubMed: 19358232]

36. Stancanello J, Terreno E, Castelli D, Cabella C, Uggeri F, Aime S. Development and validation of a smoothing-splines-based correction method for improving the analysis of CEST-MR images. Contrast Media & Molecular Imaging 2008;3(4):136. [PubMed: 18683280]

37. Sun PZ, Farrar CT, Sorensen AG. Correction for artifacts induced by B(0) and B(1) field inhomogeneities in pH-sensitive chemical exchange saturation transfer (CEST) imaging. Magnetic Resonance in Medicine 2007;58(6):1207–1215. [PubMed: 17969015]

38. Webb P, Spielman D, Macovski A. Inhomogeneity correction for in vivo spectroscopy by high-resolution water referencing. Magnetic Resonance in Medicine 1992;23(1):1–11. [PubMed: 1734171]

39. Woessner DE, Zhang S, Merritt ME, Sherry AD. Numerical solution of the Bloch equations provides insights into the optimum design of PARACEST agents for MRI. Magnetic Resonance in Medicine 2005;53(4):790–799. [PubMed: 15799055]

40. Henkelman R, Stanisz G, Graham S. Magnetization transfer in MRI: a review. NMR in Biomedicine 2001;14(2):57–64. [PubMed: 11320533]

41. Mulkern RV, Williams ML. The General-Solution to the Bloch Equation with Constant Rf and Relaxation Terms - Application to Saturation and Slice Selection. Med Phys 1993;20(1):5–13. [PubMed: 8455512]

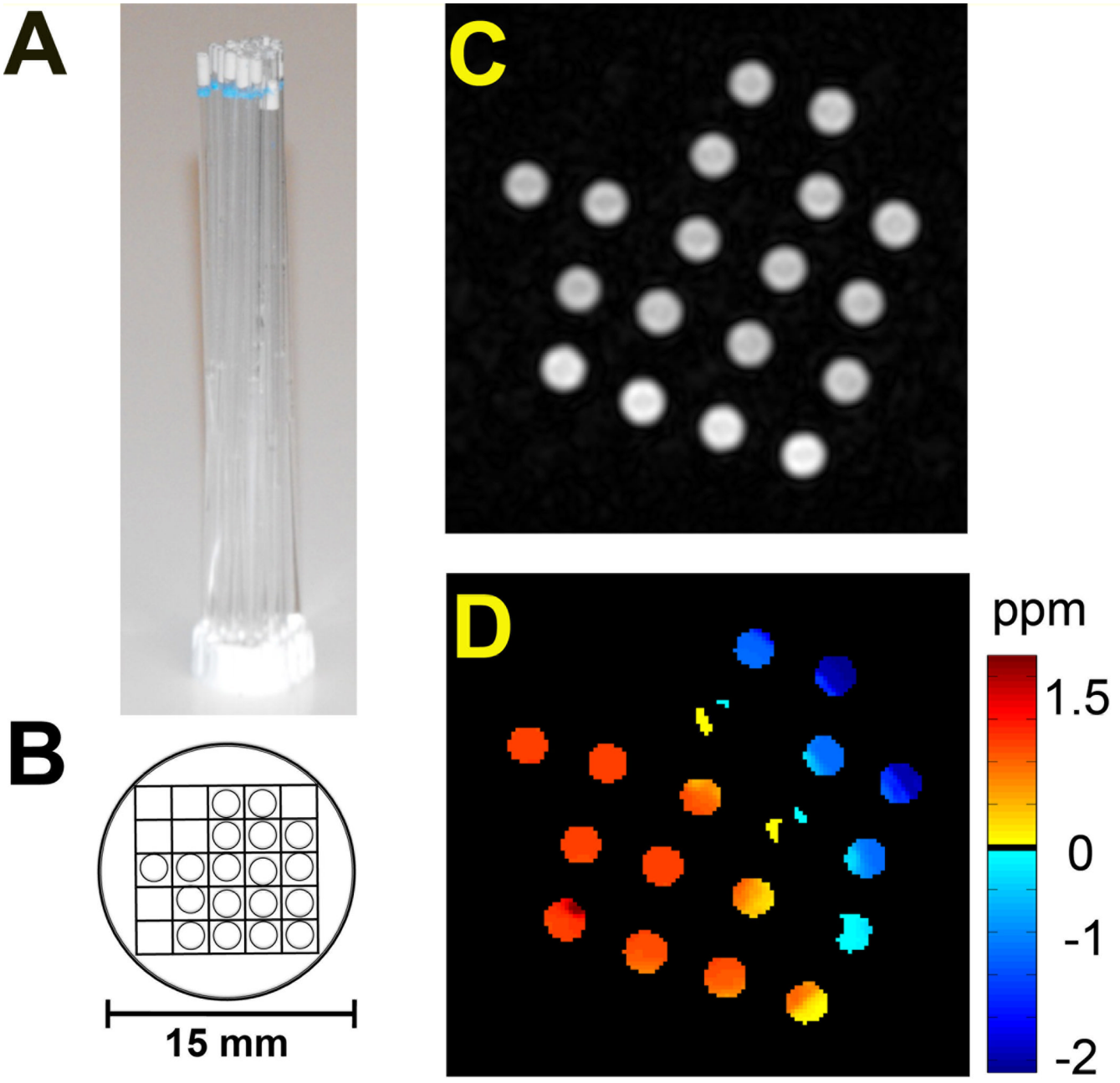

Figure 1.
Example of a high throughput sample arrangement. A) Picture of a phantom consisting of multiple capillaries immobilized in a sample holder. B) Cartoon showing anisotropic arrangement of 18 capillaries in the holder in order to easily identify the relative position of each tube in the MR images. C) An axial T_2 weighted MR image, and D) the corresponding B_0 shift map across the FOV for this phantom.

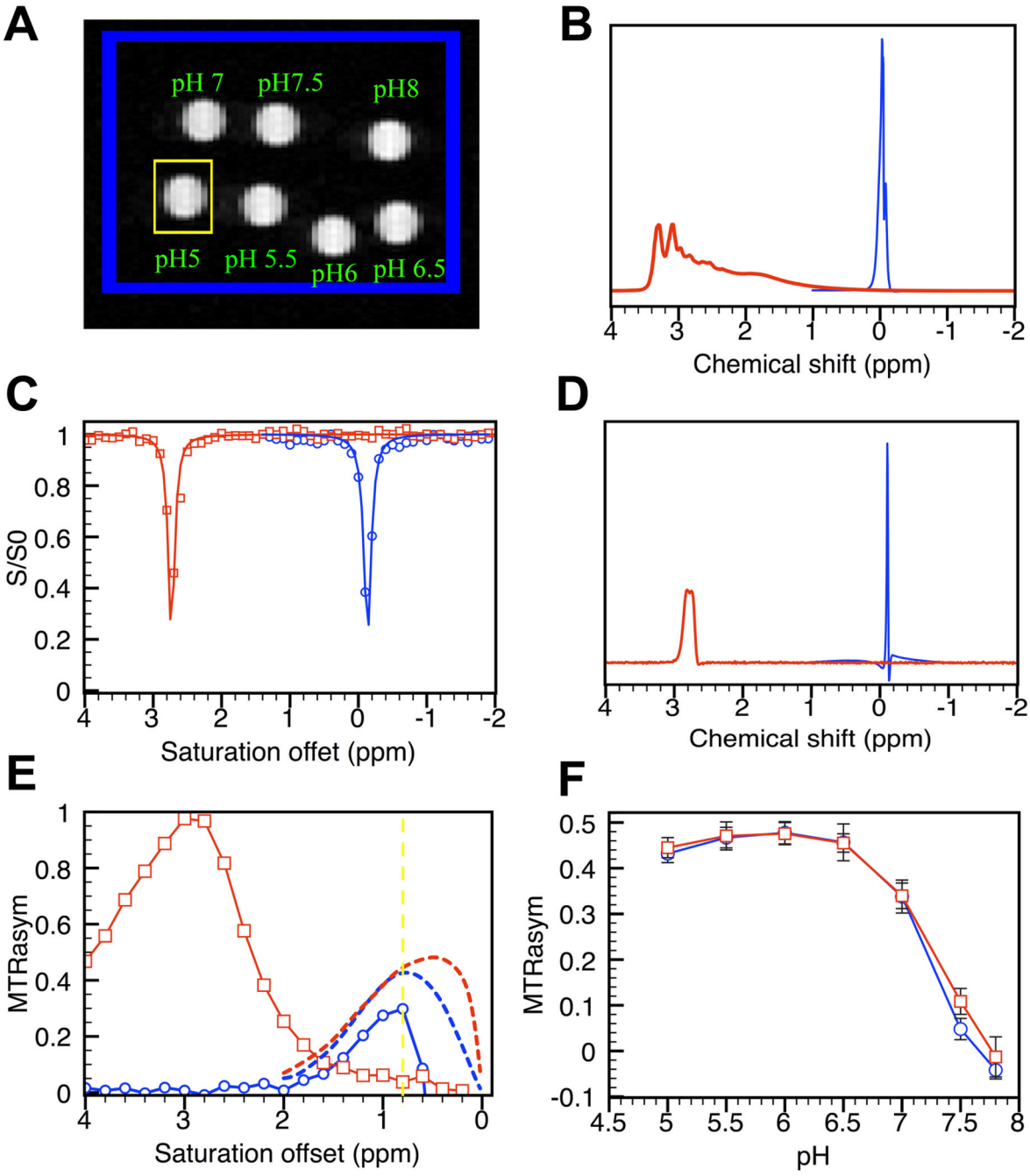

Figure 2.

Correction of B_0 inhomogeneity for a HT-CEST phantom. A) Phantom of 7 capillaries containing myo-inositol solutions (31.2 mM in PBS) with pH ranging from 5.0 to 7.8; B) Water spectra of the entire phantom under shimmed (blue line) and deshimmed (red line) conditions, C) WASSR spectra for the sample in the yellow box (pH=5.0 tube) in (A) under shimmed and deshimmed conditions; D) Water spectra for yellow box under shimmed and deshimmed conditions; E) pH = 5.0 MTR_{asym} curves for shimmed and deshimmed conditions before (solid line) and after (dashed line) B_0 correction; F) B_0-corrected pH dependency of myo-inositol CEST effects (shimmed, blue circles; deshimmed, red squares). Error bars estimated using the inter-voxel standard deviations of the ~60 voxels contained in each tube.

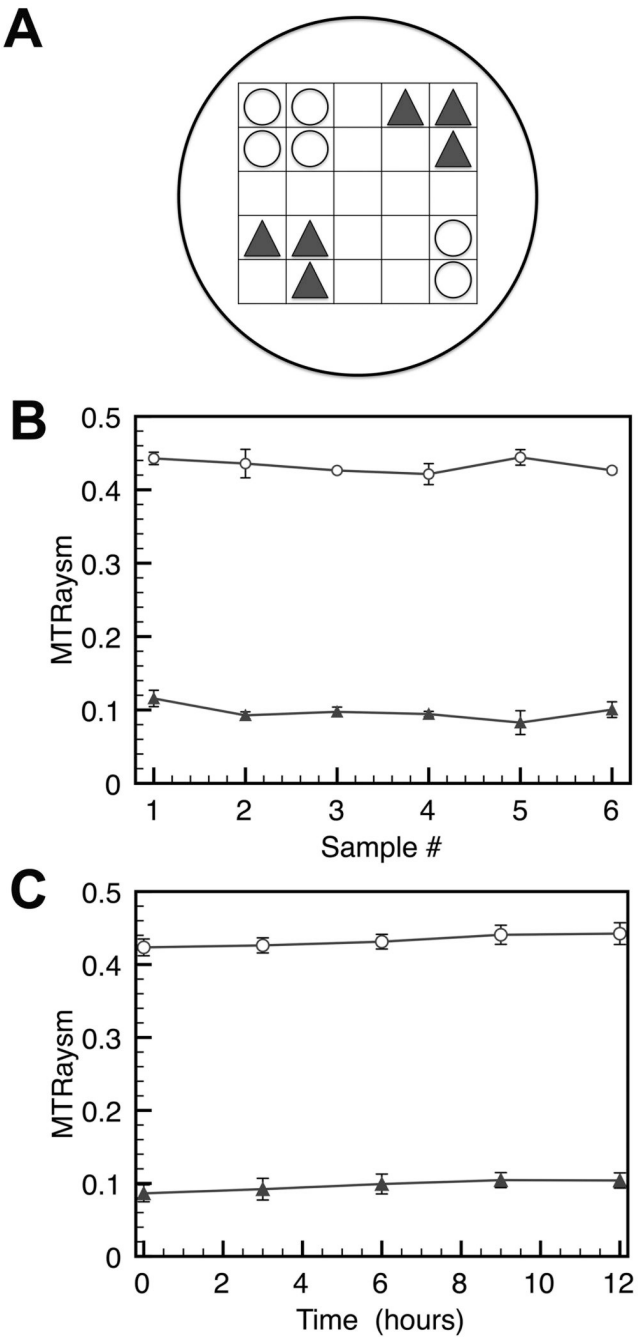

Figure 3.

Spatial variability and reproducibility of the proposed HT CEST method for six samples each of protamine sulfate (0.2 mM (▲) and 0.98 mM (□) in PBS, pH = 7.3). A) Cartoon displaying the distribution of tubes. B) Mean MTR_{asym} for each sample, with error bars showing the standard deviations of 5 measurements, C) Mean MTR_{asym} of 5 repeated independent CEST experiments with a 3 hour interval between them, with error bars showing the standard deviations over the 6 samples.

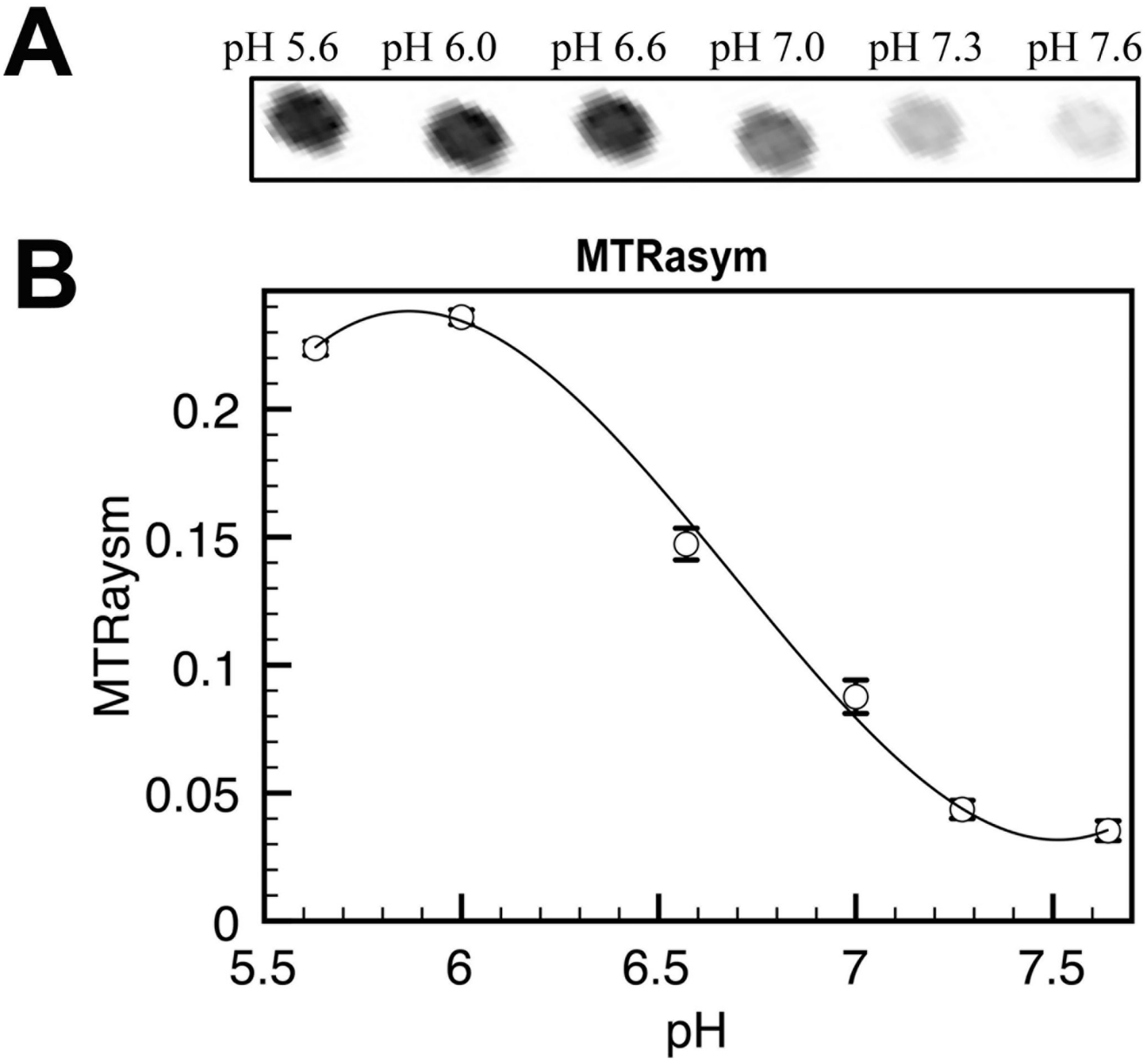

Figure 4.
The CEST properties of 20 mM uracil in PBS as a function of pH measured simultaneously using the high-throughput phantom. A) CEST contrast at 5.4 ppm as displayed by subtracting the CEST weighted image at −5.4ppm from CEST weighted image at +5.4ppm and B) the plot of MTR_{asym} as the function of pH. Error bars represent the inter-voxel standard deviations in each capillary.

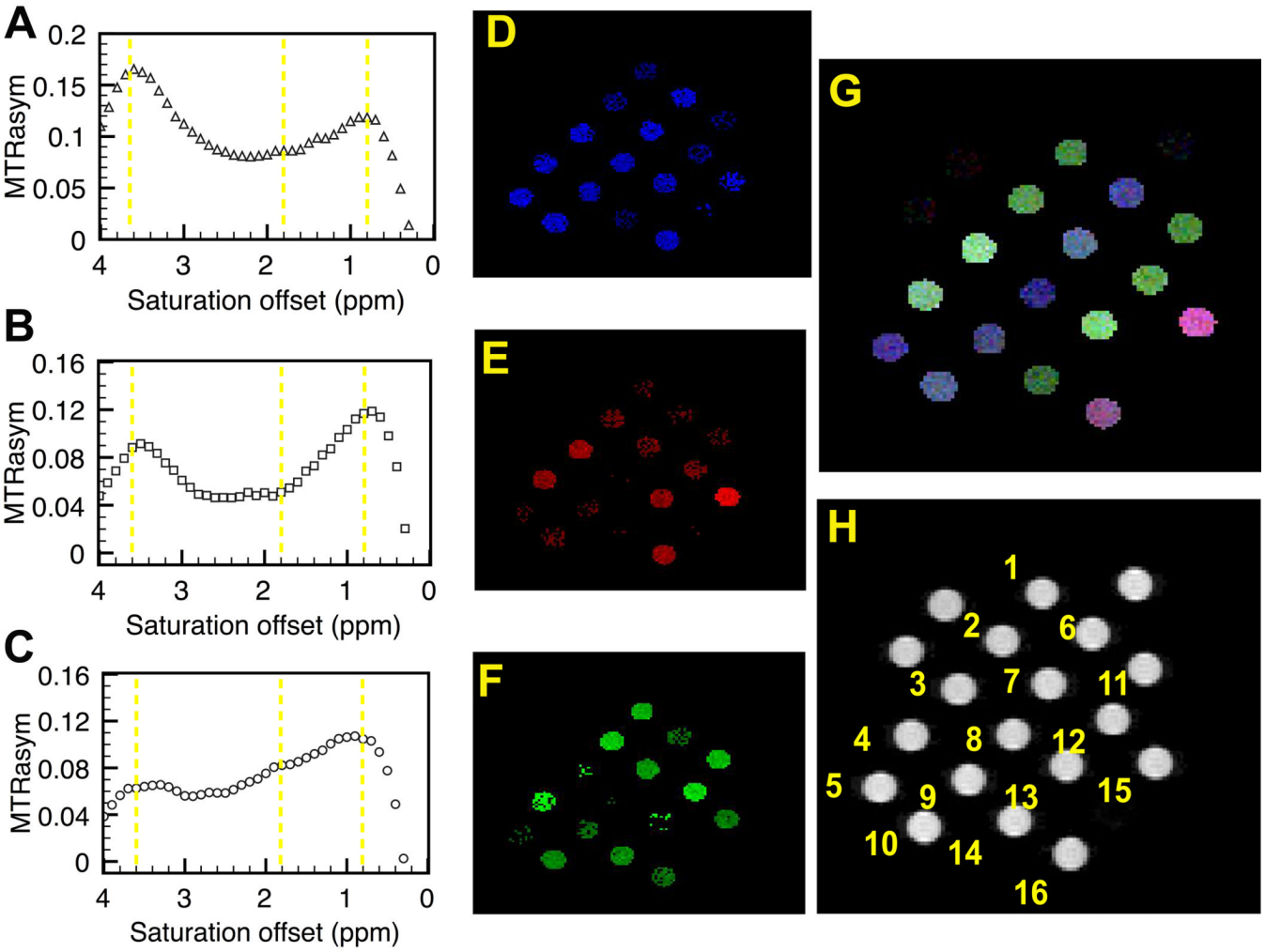

Figure 5.

High-throughput scanning of the CEST effect of 16 twelve-residue polypeptides. (A–C) CEST profiles of $(DSSS)_3$ $(DTTTTT)_2$, and $(RT)_6$. Figures D–F show the contrast at the OH (0.8 ppm, blue) NH_2 (1.8 ppm, red), and NH (3.6 ppm, green) proton frequencies, respectively. The brightness corresponds to the CEST intensity at each offset. These three-color images were overlaid to produce an 'artificial' RGB colormap (G) with the color corresponding to the summation of CEST effects at the three frequencies. In this procedure, more than 3 peptides therefore can be uniquely identified by their CEST 'footprint' in the RGB spectrum. The polypeptides were laid out as shown in the T_{2W} image (H) **1**:$(KS)_6$, **2**: $(KSSS)_3$, **3**: $(DSSS)_3$, **4**: $(DSSSSS)_2$, **5**: $(DTT)_4$, **6**: $(DTTT)_3$, **7**: $(DTTTTT)_2$, **8**: $(ETT)_4$, **9**: $(ETTT)_3$, **10**: $(ETTTTT)_2$,**11**: $(TK)_6$, **12**: $(TTK)_4$, **13**:$(TTTK)_3$, **14**: $(TTTTTK)_2$, **15**: $(RT)_6$, **16**: $(RTTT)_3$. The three unlabeled tubes contained only 10mM phosphate buffered saline. K = lysine, S = Serine, R = Arginine, T = Threonine, E = Glutamate, D = Aspartate.